Astron. Astrophys. 320, 287–299 (1997)

ASTRONOMY
AND
ASTROPHYSICS

High resolution studies of protostellar condensations in NGC 2024

H. Wiesemeyer[1], **R. Güsten**[1], **J.E. Wink**[2], **and H.W. Yorke**[3]

[1] Max-Planck-Institut für Radioastronomie, Auf dem Hügel 69, D-53121 Bonn, Germany
[2] Institut de Radio Astronomie Millimétrique, 300 Rue de la Piscine, F-38406 St. Martin d'Hères, France
[3] Institut für Astronomie und Astrophysik, Am Hubland, D-97074 Würzburg, Germany

Received 29 July 1996 / Accepted 6 September 1996

Abstract. We present interferometric $\lambda 3$ mm continuum and $C^{34}S\,(2-1)$ line observations towards the star forming NGC 2024 (south) molecular cloud core. The continuum of the prominent dust cores FIR 5 and FIR 6 is spatially resolved. FIR 5 separates into a binary or disk-envelope system.

We explore the physical characteristics of the cores by means of a radiative transfer modelling in spherical symmetry. Solutions with low bolometric luminosities ($L_{\rm bol} \sim 1-4\,L_\odot$) and massive envelopes ($M_{\rm env} \sim$ a few $10\,M_\odot$) fit the long wavelength spectral energy distributions best. Dust compositions allowing for thick ice coatings provide better agreement with the dynamical mass estimates derived from the kinematics of the surrounding gas clumps. The ambiguity of the models is severely confined by a recent $\lambda 350$ μm flux density limit from the *Heinrich-Hertz-Telescope* ($M_{\rm env} > 5\,M_\odot$, $L_{\rm bol} < 30-80\,L_\odot$). In all cases, the mass of the envelope exceeds limits on the mass of any embedded central object by order(s) of magnitude. The observations are suggestive of protostellar objects in their earliest phase of formation, with the bulk of their mass still to be accreted.

The $C^{34}S$ line emission arises from two clump ensembles near to, and likely associated with these dense cores - however, the cores proper still escape detection in their molecular emission. This striking anti-correspondence is suggestive of freeze-out of elements onto the surface of dust grains.

Key words: stars: formation – interstellar medium: dust – interstellar medium: molecules – interstellar medium: individual objects: NGC 2024 – radio continuum: ISM – radio lines: ISM

1. Introduction

The NGC 2024 H II region is located in the Orion B molecular cloud complex, as part of the extended Lynds 1630 cloud (see Lada et al. 1991, for an unbiased CS survey). Dense molecular cloud cores bracket the H II region to the north and south, and are known as sites of active star formation. Due to its relative proximity (at an adopted distance of 415 pc, Anthony-Twarog 1982) the processes of star formation can be studied in fine detail.

The discovery of seven unusually compact, ultra-dense ($n_{\rm H_2} \sim 10^8\,{\rm cm}^{-3}$) dust cores (FIR1 to FIR7) via their millimeter continuum emission by Mezger et al. (1992,1988) has stimulated a lively and controversial discussion on the true nature of these objects. While Mezger et al. analyse their data in terms of isothermally cold ($T \sim 20$ K), massive protostars, complementary IR and spectroscopic studies have questioned the early evolutionary state of the objects. Molecular outflow (FIR 4, FIR 5 and FIR 6, Sanders & Willner 1985, Richer 1990, 1992, Chandler & Carlstrom 1996) and H_2O maser activity (FIR 6, Genzel & Downes 1977, Wilson et al. 1996) was reported, which is traditionally assigned to early, but *post*-protostellar phases. But doubtless, the dynamical ages of the outflows are short ($10^3 - 10^4$ years only), and the driving sources must indeed be very young.

So far, molecular line studies have failed to detect the molecular counterparts of the dust cores: Mauersberger et al. (1992) did not find an isotopic CO counterpart to the dust condensations. The $C^{34}S$ emission (Schulz et al. 1991), albeit exhibiting a higher contrast, does not correspond to the dust emission either in position or in size. Wilson et al. (1995) concluded from their $8''$ resolution $C^{18}O\,(1-0)$ map that FIR 5 and FIR 6 are close to but not coincident with the line emission peaks. Thus, no information on the kinematics of the cores is available, and the important question, whether - as ultimate proof of their true protostellar nature - there is direct spectroscopic evidence for ongoing infall of material, remains unsettled.

Generally, the interpretation of the nature of these unique sources suffers from the limited angular resolution and sensitivity of previous studies. In this paper we present $\lambda 3$ mm continuum and $C^{34}S\,(2-1)$ line observations with $2'' \times 4''$ resolution, performed with the IRAM[1] mm-interferometer on the Plateau-de-Bure towards the cloud complex located south of the H II-region. The high resolution will enable us to discuss the morphological and kinematical fine-structure of the

Send offprint requests to: H. Wiesemeyer

[1] IRAM is a joint collaboration between the French CNRS, the German MPG, and the Spanish IGN.

complex. With the help of continuum radiative transfer models, the nature of the FIR sources will be further constrained. The anti-correspondence in the distribution between the dust and molecules will be discussed and we estimate the degree of CS depletion.

2. Instrumentation and observations

The observations were performed between January 1991 and February 1992 with the IRAM three-element interferometer on the Plateau de Bure (Guilloteau et al. 1992). The 15m antennas were equipped with two SIS-receivers and a Schottky receiver providing mean double-sideband receiver temperatures of $\sim$100 K. Observations were carried out with six different interferometer configurations, comprising baselines between 32 and 288 meters. The phase reference center was towards $(\alpha, \delta)_{1950}$ = ($5^{\rm h}39^{\rm m}13\overset{\rm s}{.}3, -1^\circ 57' 10\overset{''}{.}00$), such that both FIR 5 and FIR 6 are well within the half-power response of the antenna primary beam ($51\overset{''}{.}3$ at 96 GHz). The spectral line correlator was centered on the $C^{34}S$ $(2-1)$ transition (ν_0 = 96.413 GHz) in highest resolution mode, covering 10 MHz of bandwidth with 128 channels. The channel separation of 78 kHz corresponds to a velocity resolution of 0.24 kms^{-1}. During all observations, except for the *compact* configuration (the last one measured), the continuum correlator with 10 $\times$ 50 MHz bandwidths was operated in parallel, thus excluding any relative pointing uncertainty.

Data reduction has been carried out within the CLIC (Lucas 1992) and GRAPHIC (Guilloteau & Forveille 1992) software environment. The calibration of the visibilities was determined by means of observations of the quasars 3C84 (for bandpass and phase calibration) and 0458-020 (for amplitude calibration). Zero-spacing information obtained with the IRAM 30m-telescope has been added to the spectral line visibility data, contributing 40% to the total flux. Calibrated visibilities have been Fourier-transformed to 256$\times$256 pixel maps with $0\overset{''}{.}5$ pixel size, using natural weighting of the data. The synthesized beam of the line maps is $4\overset{''}{.}4 \times 2\overset{''}{.}4$ at position angle 18°. Due to the source position close to the celestial equator, (*u,v*) tracks are mainly oriented East-West (see insert, Fig.1), which results in a somewhat elongated clean beam with rather strong sidelobes (54 % of the peak). Best clean results were derived with interactive, combined use of the Cotton-Schwab and the Clark algorithms. The rms noise level in the final channel maps is 54 mJy/beam. The clean beam of the continuum data, lacking the compact configuration and the zero spacing correction, is slightly smaller ($3\overset{''}{.}8 \times 1\overset{''}{.}6$, 16°) due to the natural weighting of the data. The final continuum maps have an rms noise of 2.5 mJy/beam. Both sidebands (at an intermediate frequency of 1.56 GHz) have been processed separately due to the high spectral index of the dust emission, but in the following, we only have used the lower sideband (LSB) results.

Table 1. Source parameters for the 96.4 GHz continuum emission from FIR 5-e/w and FIR 6

Source	$\Delta\alpha$ [$''$]	$\Delta\delta$ [$''$]	Δa [$''$]	Δb [$''$]	P.A.	$T_{\rm b}$ [K]	S_ν [mJy]
FIR 5-w	-8.1	4.3	3.2	1.8	30°	4.5	196
FIR 5-e	-4.4	2.7	2.9	1.0	120°	2.4	53
FIR 6	4.9	-19.2	3.0	1.1	-15°	4.5	112

Notes: Offsets are relative to our phase reference center, $(\alpha, \delta)_{1950}$ = ($5^{\rm h}39^{\rm m}13\overset{\rm s}{.}3, -1^\circ 57' 10\overset{''}{.}00$); FWHP source sizes (major axis Δa, minor axis Δb) are beam deconvolved, P.A. north towards east; $T_{\rm b}$ refers to the peak brightness temperature, S_ν is the flux density of the component.

3. Results

3.1. Dust continuum emission from FIR 5 & FIR 6

While the extended dust emission is suppressed by the lack of short spacings, the continuum emission of both compact sources is clearly detected (Figs. 1 & 2). FIR 5 is resolved into a double source (hereafter FIR 5-e and -w, respectively) with a projected separation of $4''$ ($2.4 \cdot 10^{16}$ cm). Table 1 summarizes the source parameters as deduced from Gaussian model fits to the visibilities, thus avoiding uncertainties due to the irregular sampling of spatial frequencies. The visibilities of the source model (three elliptical Gaussians) were computed analytically (taking into account the interferometer primary beam attenuation) at the same spatial frequencies as those observed. The fit results were checked using the same deconvolution algorithm as applied to the observed visibilities. It is important to note that in our high resolution data, the continuum emission is spatially resolved with intrinsic size of $1'' - 3''$ (Table 1 and Fig. 2). The uncertainty in the deconvolved source sizes is estimated to $20-30$ %, while the error in the integrated fluxes is dominated by the accuracy of the absolute calibration procedure ($\sim$ 20 %).

3.2. The $C^{34}S$ *cloud cores*

The channel maps (Fig.1) reveal that the $C^{34}S$ $(2-1)$ emission from the NGC 2024 southern cloud complex separates into two clump systems near to, but not necessarily associated with FIR 5 and FIR 6 (hereafter referred as the northern clump ensemble and the southern streamer). Each of these has substructure, consisting of a number of compact, barely resolved clumps. The overall morphology is consistent with the single-dish CS data of Schulz et al. (1991), who also decomposed the complex into two subcomplexes, but whose data reveal little evidence of further substructure. It is due to the high dynamic range of this high-resolution interferometric study in the optically thin $C^{34}S$ transition, that the true underlying clumpiness is elucidated in its detail: because the high degree of clumpiness remains even after the zero-spacing correction, the observed rather smooth single-dish profiles clearly result from the superposition of narrower line contributions from an ensemble of individual clumps. This has to be accounted for when estimating virial masses (and

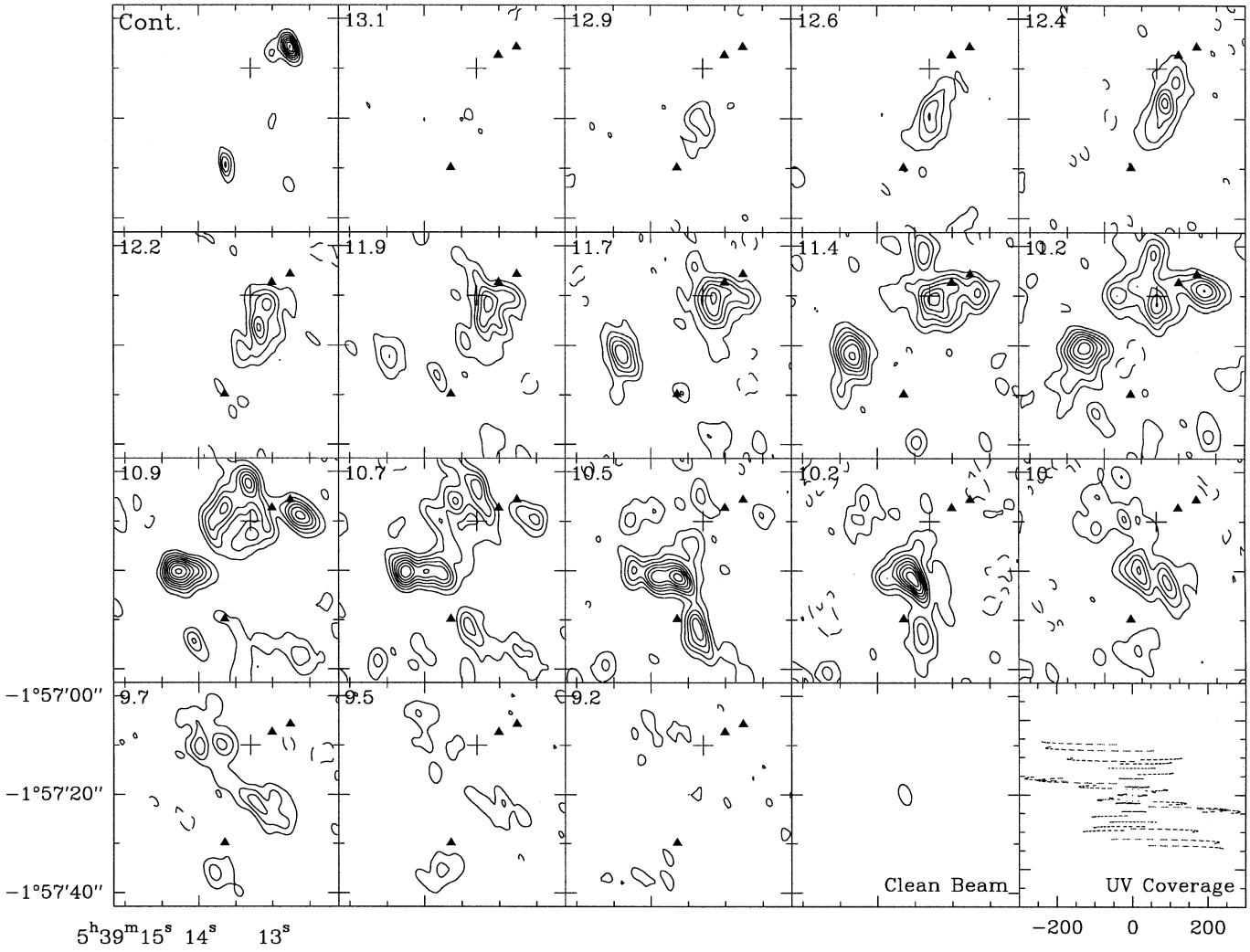

Fig. 1. $\lambda 3$ mm continuum and $C^{34}S$ $(2-1)$ line emission from the southern part of the NGC 2024 cloud core in the velocity range $v_{\rm lsr}$ = 9 to 13 km · s^{-1}. The velocity resolution is 0.24 km · s^{-1}per channel, the contours are -150, 150 to 1350 by 150 mJy/beam. The $4\farcs4 \times 2\farcs4$ clean beam (position angle 18°) and the uv-coverage are shown as an insert (bottom right). The 150 mJy contour spacing corresponds to $\Delta T_{\rm mb}$ = 1.9 K. The triangles indicate the positions of FIR 5 and FIR 6. The top-left panel shows the continuum emission (LSB, beam: $3\farcs8 \times 1\farcs6$, p.a. = 16°, level spacing 10 mJy). The cross marks the phase reference center, $(\alpha, \delta)_{1950}$ = ($5^{\rm h}39^{\rm m}13\overset{\rm s}{.}3$, $-1°57'10\farcs00$).

determining abundances with them) from lower resolution observations, which cannot separate the clumps of an ensemble (see also Section 4.1). Each of the subcomplexes shows a distinct velocity pattern: south of the phase reference center, an arc of gas encircles FIR 6 with evidence of a highly coherent velocity field - the feature is suggestive of a torus surrounding the source. In contrast, the velocity field of the northern complex is dominated by a large clump-to-clump velocity dispersion within the ensemble, with a weak underlying N-NE to S-SW velocity gradient.

Although the velocity components seen by Barnes & Crutcher (1990) in HCO^+ $(1-0)$ emission can be identified with features in our $C^{34}S$ map, their model of an expanding torus comprising both the northern clump ensemble and the southern streamer is inconsistent with our data. This is partly due to our higher resolution, but likely also due to radiative transfer effects concerning the optically thick HCO^+ line. Similarly, much of the difference in the clouds' morphologies as measured in the CS $(2-1)$ main isotope emission (Chandler & Carlstrom 1996, their Fig. 2) compared to the isotopic $C^{34}S$ line (this data, convolved to OVRO beam) is due to the transition's large opacity. Ignoring details of excitation, main beam brightness temperature ratios $T(\mathrm{CS})/T(\mathrm{C^{34}S})$ as small as 1.3 are observed towards their positions $3-5$, implying main line center optical depths of order ~ 10 (assuming $^{32}S/^{34}S$ = 23). The CS main line profiles are broader than those in the ^{34}S isotopomer by a factor ~ 2 (Table 2), which again can be accounted for by the large opacity: for a Gaussian line shape, a line center optical depth of 10 will broaden the profile by a factor of 2.

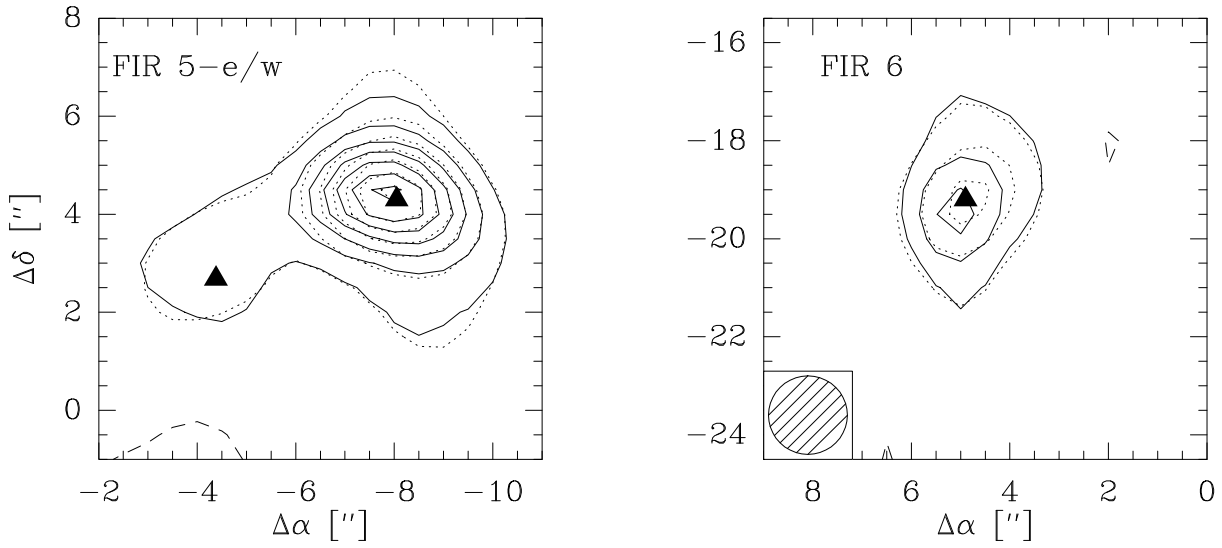

Fig. 2. Comparison between the observed (dotted contours) and the modelled (solid contours) flux density distribution of FIR 5-e/w and FIR 6. Contours spacing is 10 mJy/beam, a circular clean beam (insert) of 1.″6 has been used to get a sensitive fit result. Residuals are weaker than 4 mJy/beam.

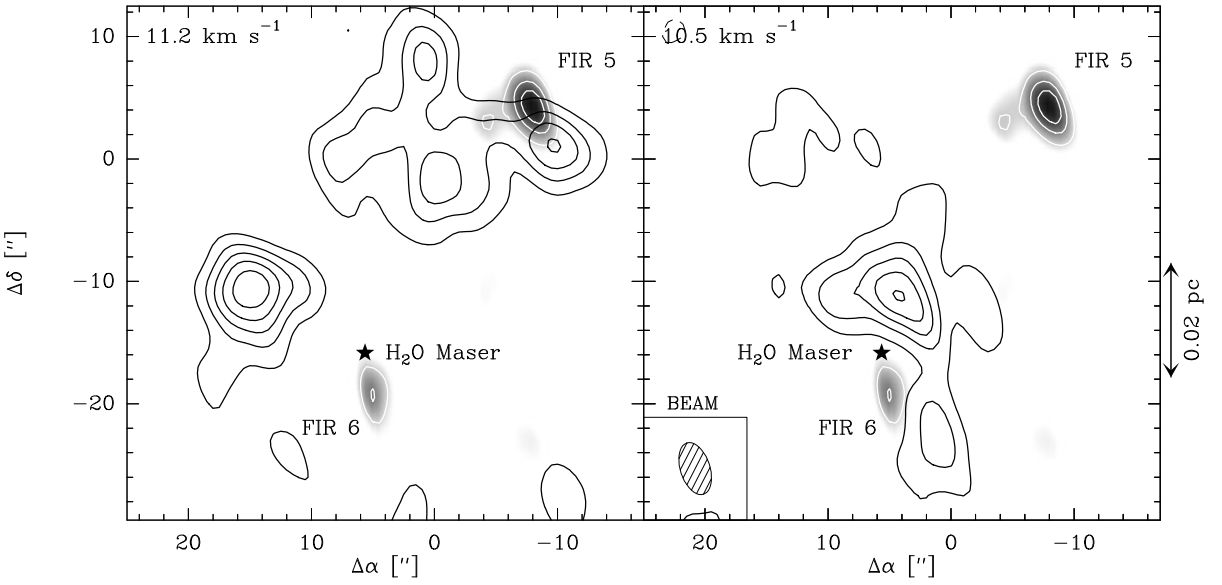

Fig. 3. λ3 mm continuum emission from the FIR 5 and FIR 6 dust cores (greyscale). The contours (spacing 2.5 K) show the $C^{34}S$ (2 – 1) emission, averaged from 10.9 to 11.4 kms^{-1} (left) and 10.2 to 10.7 kms^{-1} (right). The asterisk denotes the VLA position of the H_2O maser (T.L. Wilson, priv. communication).

A closer inspection of the channel maps (Fig.1) reveals no direct morphological correlation between the $C^{34}S$ line and the continuum emission (Fig. 1, 3) - none of the two compact FIR cores observed shows associated $C^{34}S$ line emission, and vice versa, no dust counterpart to the dense CS clumps has been detected. We will discuss these findings in the following subsections.

4. Discussion

4.1. The $C^{34}S$ *cloud cores: physical characteristics*

In order to determine the physical conditions in the cloud cores, we decomposed the observed emission into individual clumps, using the GAUSSCLUMPS procedure developed by Stutzki & Güsten (1990). GAUSSCLUMPS is an iterative least-square algorithm to fit two-dimensional Gaussians to the observed brightness distribution. The deconvolution from the elongated elliptical beam was performed by means of the Fourier transform

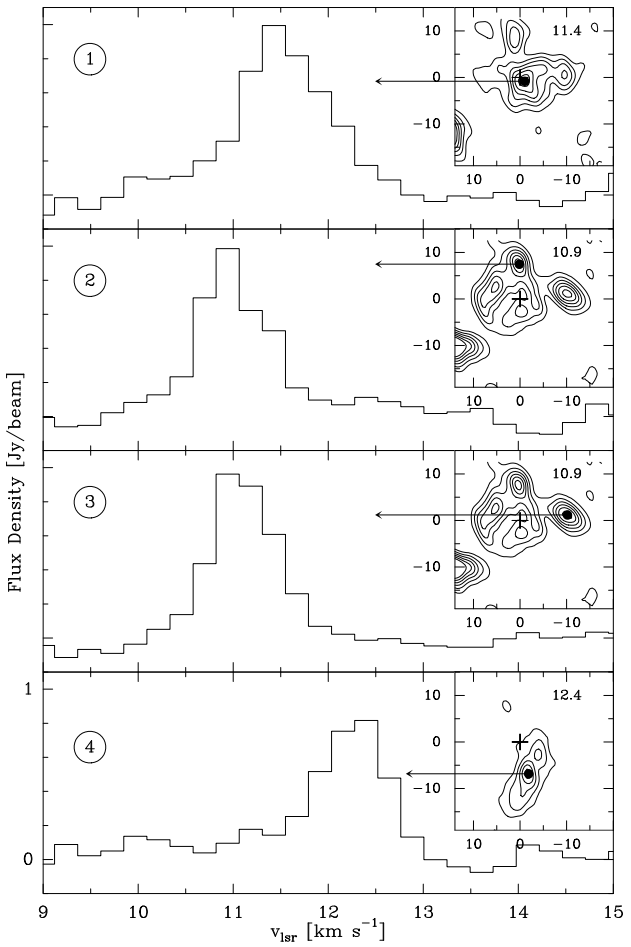

Fig. 4. Spectra and channel maps (inserts, box marking: $v_{\rm lsr}$) for some of the prominent clumps, showing the fine-structure of the NGC 2024 cloud core in velocity space; contour spacing and clean beam as in Fig. 1. The spectra shown (numbering according to Table 2) are extracted at the clump maxima. The offsets (in $''$) are relative to the phase reference center, marked by a cross.

convolution theorem, making use of the commutability of the two-dimensional Fourier transformation and rotations.

4.1.1. The northern clump ensemble

Table 2 summarizes the results for the five most prominent clumps in the northern clump ensemble. Typical (intrinsic) clump sizes are 1000-2000 AU only, the $C^{34}S\,(2-1)$ lines are narrow ($\Delta v_{\rm FWHM} \sim 0.5$ km $\cdot$ s^{-1}, Mach number ~ 1). Assuming that the individual clump is in virial equilibrium, H_2 densities are derived that range between 10^6 and 10^7 cm^{-3}, and compare nicely with the (mass-) averaged densities for the overall complex deduced by Schulz et al. (1991) in their single-dish CS excitation analysis.

In the following, we describe the excitation by means of an escape probability technique, assuming a uniform-density, isothermal sphere (at $T_{\rm kin} \sim 35$ K, cf. Table 4. of Schulz et al. 1991), as described by Goldreich & Kwan (1974). The individual clump's virial masses, a few 0.1 $M_\odot$, are used to fix the $C^{34}S$ molecular abundance, $X(C^{34}S) = (8.6 \pm 3.8) \times 10^{-10}$, which thus appears enhanced by factors of 8 (Blake et al. 1987) and 2 (Sutton et al. 1995) as compared to the fractional abundance determined for the OMC 1 extended ridge. Table 2 gives the virial masses for different assumptions (the gravitational potential of ellipsoidal clouds is deduced in Bertoldi & McKee 1992, complications of the virial theorem due to surface pressure, magnetic fields, and a non-uniform density distribution lead to an order unity correction, for details see McKee & Zweibel 1992).

The clump masses sum up to a total of $\sum m_{\rm cl} \sim 1 M_\odot$, which compares well with total gas mass estimates based on the column density tracing $C^{18}O\,(1-0)$ data presented by Wilson et al. (1995, for their clump $C^{18}O{-}5$, we calculate 1.4 $M_\odot$, using $T_{\rm kin} \sim 35$ K and [CO] $\sim 10^{-4}$). However, a core gas mass that small falls significantly short of the dynamical mass $M_{\rm dyn}$, estimated from the *interclump* velocity dispersion within the ensemble (assuming a homogeneous distribution of clumps with line-of-sight velocity v_i and mean velocity $\bar{v}$):

$$\frac{3}{5} \cdot \frac{G \cdot M_{\rm dyn}}{R_{\rm proj} \cdot \frac{\pi}{2}} = 3 \cdot \sigma_v^2 = 3 \cdot \frac{1}{N_{\rm cl} - 1} \sum_{i=1}^{N_{\rm cl}} (v_i - \bar{v})^2, \qquad (1)$$

where $R_{\rm proj}$ is the maximum (projected) cluster radius. With $\sigma_v = (0.55 \pm 0.10)$ km $\cdot$ s^{-1} (for the five most massive clumps, comprising 73% of the total velocity integrated flux density) and $R_{\rm proj} \sim 10''$, we calculate $M_{\rm dyn} = (12 \pm 7)\ M_\odot$.

This order of magnitude discrepancy relative to the *observed* gas mass could partly be explained if the ensemble were not virialized (e.g. due to an interaction with the outflow), but may also be used to limit the amount of *hidden* mass, that is not traced by the $C^{34}S\,(2-1)$ or the $C^{18}O\,(1-0)$ transitions. One possibility is that the mass of nearby FIR 5 (see Section 4.2) can account for the extra potential required to model the observed velocity dispersion - or in other words, we suggest that in fact the continuum core(s) are (1) massive and (2) physically interacting with the (gas) clump ensemble. Within this scenario it can now be explained why virial mass estimates based on lower resolution observations (e.g. Schulz et al. 1991, Wilson et al. 1995), which do not resolve the clump ensemble, typically exceed the clump gas masses $\sum m_{\rm cl}$ deduced here by an order of magnitude: low spatial resolution leads to a spectral blend of the clumps' emission, and thus synthesizes a linewidth which is more likely to reflect the interclump velocity dispersion than the turbulent and thermal linewidth of individual clumps. Such a mass estimate is close to the approach given by Eq. (1), thus including any hidden mass.

4.1.2. The southern streamer

The velocity structure of the gas surrounding FIR 6, which is located within a well-defined cavity void of $C^{34}S$ emission, is highly coherent and suggestive of an eccentric, partial torus in orbit around the source (see e.g. the striking ridge in the channel maps of Fig. 1, starting $\sim 10''$ north of the FIR 6 core

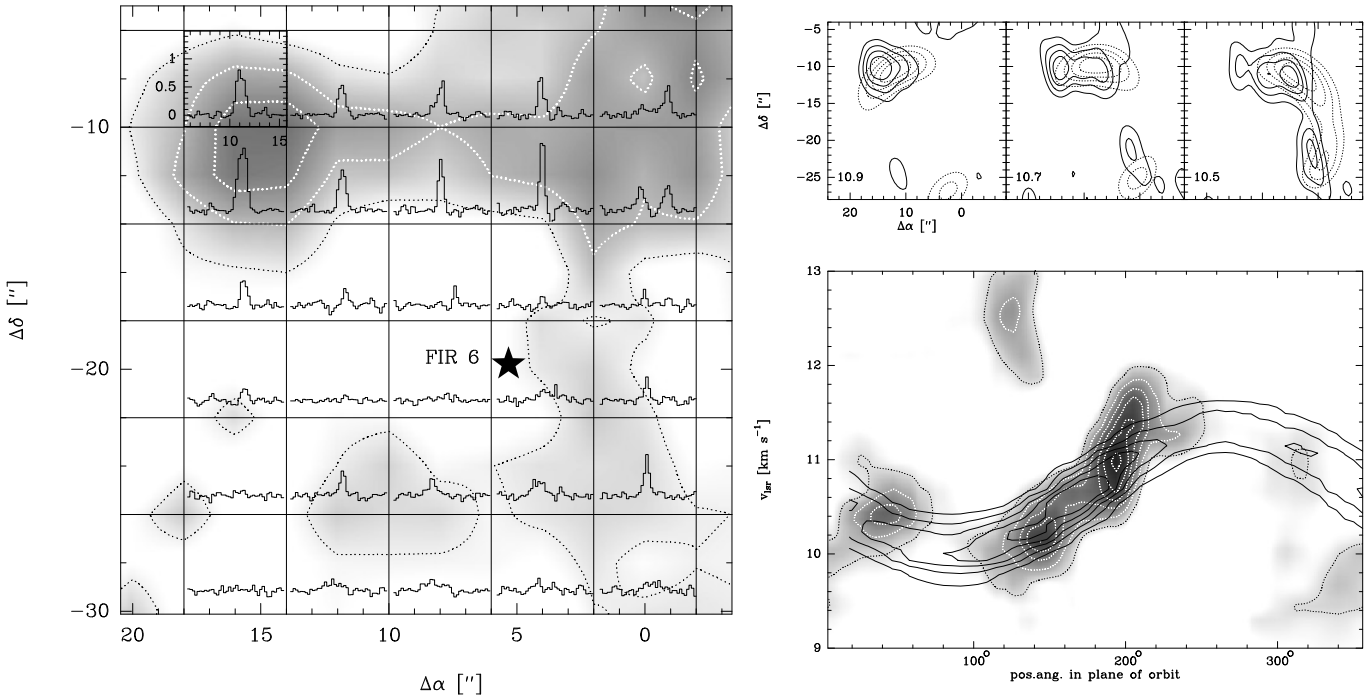

Fig. 5. Left: $C^{34}S$ spectra towards the *streamer*, superposed on a grey scale representation (dotted contours at 25, 50 and 75%) of the velocity-integrated ($v_{\rm lsr}$ = 8.3 − 13.4 km s^{-1}) $C^{34}S$ (2 − 1) emission around FIR 6 (marked by a star). The $v_{\rm lsr}$ [km s^{-1}] and Jy/beam ranges are indicated in the upper left box. Position offsets are relative to the phase reference center. Note that the spectra in the north-western quadrant show two velocity components, the feature at higher velocities is part of the northern complex. **Upper right:** Overlay of the observed and modelled (dashed contours) $C^{34}S$ (2 − 1) emission (box marking: $v_{\rm lsr}$, bottom left). Contours are 20 to 80 % by 20 % (0.25 to 1.0 by 0.25 Jy/beam). **Lower right:** Position-velocity-cut *along* the streamer (grey scale, dotted contours at 0.2 Jy/beam level spacing), projected onto the plane of orbit, in order to elucidate the sine-wave pattern after appropriate weighting by the primary beam response.

and bending east to west and south). It can be best seen in the velocity integrated $C^{34}S$ emission around FIR 6 (Fig. 5a). A position-velocity-diagram *along* the streamer (Fig. 5b) reveals a well-defined sinusoidal pattern, characteristic of a rotating ring structure seen in projection against the plane of the sky. A model fit is superposed for a gas torus of constant density. Its geometry is described by the major axes of the inner and outer orbits (of the same eccentricity) and by an elliptical cross-section. Its kinematic is described in terms of a Keplerian orbit. The modelled $C^{34}S$ (2 − 1) emission, constrained to fit the observed emission pattern in each velocity channel, is derived for a $T_{\rm kin}$ = 35 K gas, using the same escape probability technique as in the analysis of the northern ensemble. Its distribution in velocity space fits the basic characteristics of the observed features, i.e. the line-of-sight velocities and the emission enhancement due to velocity crowding. Residuals are due to the streamer's internal clumping, which is not considered by the model. Table 3 summarizes the details of the model.

Within the uncertainty of our simple model, the fitted center of gravity falls close to the position of FIR 6 (Table 1). A comparison of the compact outflow lobes (Richer 1990, Chandler & Carlstrom 1996) with the model maps of Cabrit and Bertout (1986) suggests that the outflow axis makes a large angle with the plane of the sky, such that the plane of the streamer is perpendicular to the outflow.

The dynamical mass deduced, $M_{\rm dyn} \sim 25$ M$_\odot$, again exceeds by order of magnitude the "visible" mass traced by the $C^{34}S$ emission ($M_{\rm gas} \sim 2$ M$_\odot$, assuming a fully thermalized level population at $T_{\rm kin}$ = 35 K, and for the fractional $C^{34}S$ abundance determined for the northern complex), and requires a massive central object. The streamer mass is low as compared to this estimate, thus justifying to model its dynamics with a Keplerian orbit and neglecting its self-gravity. Therefore, although based on a different dynamical approach, we conclude that FIR 6 must be also massive. The next subsection will address the question whether this excess mass is located in the dust core or in a central young stellar object.

4.2. The dust cores: physical characteristics

First we will characterize the nature of the dust condensations following the simple (analytical) approach of an isothermal sphere of constant density. In a complementary and more consistent approach, the emission of the protostellar dust cocoon will be modelled using the RADTR code developed by Yorke (1980) which self-consistently solves for the equation of radiative transfer in spherical geometry. We restrict this analysis to the case of FIR 5-w, which is resolved at λ3 mm. The contribution from FIR 5-e to the observed total flux is within the

Table 2. $C^{34}S$ clump characteristics (northern complex)

clump label	1	2	3	4	5
$(\Delta\alpha, \Delta\delta)_{1950}$ [″]	(-1.5,-1.0)	(0.7,7.4)	(-10.0,1.0)	(-1.8,7.1)	(5.7,2.0)
clump velocity [km $\cdot$ s^{-1}]	11.5	10.9	11.1	12.3	11.0
clump size [″]					
major axis	5.6	4.2	4.5	7.1	6.5
minor axis	4.3	3.1	2.5	2.4	3.0
position angle	-33	-13	90	-34	30
linewidth [km s^{-1}]	0.69	0.49	0.57	0.57	0.40
$T_{\rm line}$ [K]	17	23	31	20	18
$n_{\rm H_2}$ = const.					
virial mass [$M_\odot$], prolate ellipsoid	0.6	0.4	0.3	0.3	0.3
oblate ellipsoid	0.7	0.5	0.5	0.8	0.7
mean density $\langle n_{\rm H_2}\rangle_{\rm V}$ [10^7 cm^{-3}]	0.4	0.3	0.5	0.3	0.1
$n_{\rm H_2} \propto r^{-2}$					
virial mass [$M_\odot$], prolate ellipsoid	0.3	0.2	0.2	0.2	0.2
oblate ellipsoid	0.4	0.3	0.3	0.5	0.4
mean density $\langle n_{\rm H_2}\rangle_{\rm V}$ [10^7 cm^{-3}]	0.6	0.6	0.8	0.4	0.2
$C^{34}S$ mass [$M_\odot \times 10^{-9}$]	0.3	0.2	0.6	0.2	0.1
peak col. density $N_{\rm H_2}$ [10^{23} cm^{-2}]	1.4	1.9	7.5	1.5	0.9
dynamical mass of northern complex	$\sim 12\ M_\odot$				

Notes: Source parameters as deduced from GAUSSCLUMPS. Position offsets $(\Delta\alpha, \Delta\delta)$ are relative to the phase reference center. Clump sizes and line brightness temperatures have been deconvolved from the clean beam ($2\farcs4 \times 4\farcs4, 18^\circ$). Linewidths (FWHM) are corrected for the (finite) correlator response function and thermal broadening (for $T_{\rm kin}$ = 35 K). Virial (total gas) masses and mean H_2 densities (for solar metallicity) are deduced assuming that the individual clump is in virial equilibrium. Peak column densities and $C^{34}S$ masses are derived from an excitation analysis based on an escape probability technique.

FIR 5 flux uncertainty. The observational constraints that must be satisfied are as follows:

- The VLA λ1.3 cm data of Gaume et al. (1992, clean beam: $3\farcs8 \times 3\farcs2$) show no evidence for the dust condensations seen at mm wavelengths. For the source size as derived above (Table 1), we infer an upper limit of $3\sigma_{\rm rms} \simeq 3$ mJy. This excludes the possibility of a flat spectral index and confirms the nature of the continuum emission as due to dust.
- An extremely valuable constraint from our interferometer data is that the intrinsic source size at λ3 mm has been determined, thus providing a direct estimate of the optical depth at this wavelength. In the following, we model the source such that the area from which half of the flux density is emitted equals the area within the half-power contour of the Gaussian profiles (FWHP $\simeq 2''$, as deduced from the visibility data). Note that due to the sensitivity of the interferometer response to small-scale structure, no confusion due to background emission falsifies the intrinsic core emission.
- The IRAM 30m telescope measured continuum flux densities at λ870 μm and λ1300 μm (Mezger et al. 1988, 1992). The emission plateau that appears only in the single dish observations is subtracted from the λ1300 μm map. The FIR 5-e/w components are assumed to be unresolved by the $10''$ beam. The higher resolution λ870 μm observations allowed a fit of Gaussians to the dust emission and to subtract simultaneously an emission pedestal (using the AIPS software package IMFIT procedure). The resulting flux densities are at λ870 μm 7.9 Jy for FIR 5 and 3.1 Jy for FIR 6, and at λ1300 μm 4.5 Jy and 0.9 Jy, respectively.
- Neither FIR 5 nor FIR 6 are detected at 2.2 μm (K-band map by Barnes et al. 1989). KAO observations at 40, 60, 100 and 160μm (Thronson et al. 1984) detected hot dust associated with the H II region, but there is no evidence for a (unlikely) contribution from FIR 5.

4.2.1. The isothermal model (analytical approach)

IF the dust temperature $T_{\rm D}$ across the - so assumed - isothermal sphere were known, then, with the intrinsic source solid angle $\Omega_{\rm s}$ deduced from our interferometry (Table 1), the dust opacity is directly determined by the measured source flux density via the antenna equation,

$$S_\nu = \int_{\Omega_{\rm S}} B_\nu(T_{\rm D}) \cdot (1 - e^{-\tau_\nu}) d\Omega, \qquad (2)$$

which reads, for the assumed geometry,

$$S_\nu = B_\nu(T_{\rm D})\Omega_{\rm S} \cdot \left(1 + \frac{2}{\tau_\nu} e^{-\tau_\nu} + \frac{2}{\tau_\nu^2}\left(e^{-\tau_\nu} - 1\right)\right), \qquad (3)$$

where τ_ν denotes the opacity of the central line of sight. Unfortunately, with the data points at hand, the dust temperature

Table 3. Model fit parameters for the streamer around FIR 6

characteristic sizes	
inner radius [pc]	0.016
outer radius [pc]	0.024
height [pc]	0.008
characteristics of Keplerian orbit	
inclination	75°
position angle	30°
eccentricity	0.4
period [yr]	$3.8 \cdot 10^4$
periastron position angle	110°
$\Delta\alpha$ (c.o.g.)	8″
$\Delta\delta$ (c.o.g.)	-19″
physical characteristics	
$n_{\mathrm{H_2}}$ [cm^{-3}]	2×10^6
linewidth (FWHM) [km $\cdot$ s^{-1}]	0.4
dynamical mass [M$_\odot$]	$\lesssim 25$
streamer gas mass [M$_\odot$]	2

Notes:
Parameters are chosen to fit the observed $C^{34}S$ $(2-1)$ emission (modelled emission from escape-probability approach). Inclination and position angle are given for the angular momentum vector (from sky plane to observer, north towards east). Center of gravity (c.o.g.) coordinates are specified with respect to the phase reference center. The total mass is derived from a dynamical mass estimate and comprises the streamer and FIR 6 masses. The mass of the streamer is derived from the $C^{34}S$ $(2-1)$ observations, assuming a fully thermalized (T_{kin} = 35 K) level population and a fractional $C^{34}S$ abundance of 9.0×10^{-10}.

is not well constrained and depends heavily on the assumed wavelength dependence of the dust extinction coefficient. In fact, much of the dispute in the literature about the true nature of these dust cores relates to the uncertainty about this relation, i.e. whether $\tau_\nu \propto \nu^2$ (as proposed by Mezger et al. 1990) or $\tau_\nu \propto \nu$ (used by Chandler & Carlstrom 1996). For example: from the comparison of the 90 and 345 GHz fluxes, we constrain a dust color temperature of T_{D} = 15 K for $\tau_\nu \propto \nu^2$, while for $\tau_\nu \propto \nu$, T_{D} is basically undetermined (even solutions with T_{D} a few 100 K fit the sub-mm data).

For the model calculations presented in the next section, the dust opacity is no longer a free parameter, but is defined by the dust composition and the density structure chosen (see below). For reference, we first discuss the data in terms of an isothermal, constant density dust sphere. Using the quasi-empirical dust extinction cross section per hydrogen nucleus, $\sigma_\lambda^{\mathrm{H}}$, given by Mezger et al. (1990), and the λ3.1 mm opacity determined via Eq. (2), the total hydrogen column density is easily calculated:

$$N_{\mathrm{H}}[\mathrm{cm}^{-2}] = \tau_\lambda / \sigma_\lambda^{\mathrm{H}} = 4.1 \cdot 10^{26} \cdot \tau_{\lambda 3.1\mathrm{mm}}, \quad (4)$$

for solar metallicity and gas of high density (scaling the opacity of the diffuse interstellar gas by a factor of 3.4). Results of our fits are summarized in Table 4 and Fig. 6, and indicate extremely high column densities and volume densities, with envelope masses between 12 (FIR 5-e) and 45 (FIR 5-w) M$_\odot$.

4.2.2. Radiative transfer models of the FIR 5-w dust cocoon

Next, in a physically more consistent approach, we will model the emission of the protostellar envelope, using the RADTR code and a realistic dust model. The models allow for radial density gradients, $n \propto r^{-s}$, and solve for the temperature structure self-consistently. The (internal) heating is maintained by a central black body source. Its temperature has little influence on the resulting spectral energy distribution (SED) within a wide range, because the radiation field at the inner radius of the dust envelope is rapidly converted by the dust into a radiation field at lower temperature (see Yorke and Shustov 1981). In the following, we adopted T_{eff} = 4800 K. In the non-grey case, the dust temperature is governed by the equilibrium condition

$$\int_0^\infty Q_\nu^{\mathrm{abs}} (B_\nu(T) - J_\nu) d\nu = 0, \quad (5)$$

where the grain size averaged absorption coefficient is denoted by Q_ν^{abs}, the Planck function at temperature T by $B_\nu(T)$, and the zero$^{\mathrm{th}}$ moment of the radiation field by J_ν. Because of the coupling between the dust temperature and - implicitely - the optical properties of the dust grains, the code has to determine the dust sublimation radii iteratively. The outer boundary condition to the inwards directed intensity component is an undiluted 3 K blackbody radiation field.

The dust is characterized in terms of the three component model by Preibisch et al. (1993), taking into account that, under the conditions in dense cloud cores, the optical properties of dust grains are likely modified by ice coatings. The sublimation temperatures are uncertain. However, Preibisch (1992) showed that a variation of up to 50% does not lead to significant changes in the SED. The main features of the dust model, that consists of amorphous carbon grains (aC), astronomical silicates (Si), and ice-coated silicate cores (core-mantle-particles, CMP) are summarized in Table 5 (for details, see Preibisch et al. 1993).

Table 6 summarizes the characteristics of the models performed, covering a wide range of ice coatings and density profiles ($n \propto r^{-s}, 1 \leq s \leq 2$). The envelope mass M_{env}, the outer radius R_{out}, and the central source luminosity have been fit to match the observed spectral energy distribution (SED) *and* the λ3 mm source size. Due to the high opacity shortwards of sub-mm wavelength, 900 grid points at equidistant logarithmic spacing have been used for the more massive models (and 300, respectively, for the less massive ones), in order to ensure convergence. The dust models yield long wavelength extinction cross-sections of $\kappa_{1.3\mathrm{mm}} = 2 \times 10^{-3}$ to 0.01 cm^{2}g^{-1} (Table 5), that encompass more or less those used by Mezger et al. (1990, $\kappa_{1.3\mathrm{mm}} = 7 \times 10^{-3}$ cm^{2}g^{-1}) and Beckwith et al. (1990, $\kappa_{1.3\mathrm{mm}} = 0.02$ cm^{2}g^{-1}). The frequency dependence of the mass extinction coefficient $d \log \kappa_\nu^{\mathrm{ext}} / d \log \nu$, is $\sim$ 1.5 (Table 5, but note that due to optical depth effects even at mm wavelengths the *observed* opacity index may be much lower, see Table 6). Even more, the observed spectral index is predicted to flatten towards to central line-of-sight of the dust core, where the brightness observed at longer wavelenghts - sampling all the material, including warm nuclear shells - may even exceed the brightness

Table 4. FIR 5 model results for an isothermal sphere at constant density [(1)].

Source	$R_{\rm out}$ 10^{16} cm	$\Omega_{\rm S}^{(2)}$ [arcsec^2]	$\tau_{\rm 3mm}^{(3)}$	$N_{\rm H_2}^{(4)}$ [10^{25}cm^{-2}]	$n_{\rm H_2}$ [10^9cm^{-3}]	$M_{\rm env}^{(5)}$ [M$_\odot$]	$L_{\rm bol}$ [L$_\odot$]
FIR 5-w	1.2	12.3	0.16	6.4	2.6	45	1.4
FIR 5-e	0.9	8.7	0.08	3.3	1.9	12	0.7
FIR 6	0.9	9.3	0.16	6.3	3.4	26	0.8

Notes: [(1)] Isothermal envelope at $T_{\rm D}$ = 15 K and constant density; [(2)] Ω_S denotes the intrinsic source solid angle; [(3)] λ3 mm opacities from Eq. (3) ($\tau_\nu \propto \nu^2$); [(4)] column densities are peak values; [(5)] total masses are given for solar metallicity.

Table 5. Main features of the ice-coated silicate particles (CMP)[(1)]

model	coating thickness			$T_{\rm CMP}$	ice pollution	$\kappa_{\rm 1.3mm}^{\rm ext}$ [(2)]	$\frac{\Delta(\log(\kappa_\nu^{\rm ext}))}{\Delta(\log(\nu))}$ [(3)]
	$c_{\rm min}$	$c_{\rm max}$	size distribution		by aC grains	[10^{-3} cm^{2}g^{-1}]	
	[μm]		(power law index)	[K]	(vol%)		
A	0.008	0.2	-3.5	125	10%	3.1	1.4
B	0.040	1.0	-3.5			10.5	1.5
C	0.003		0.0			2.2	1.4
D	0.045		0.0			6.4	1.5

Notes: [(1)] Below $T_{\rm CMP}$, all Si grains have ice-coatings, polluted by aC grains. The size distribution of aC and Si grains follows a power law in the form $n(a) \propto a^{-3.5}$ (Mathis et al. 1977), with cutoff radii 7nm $\leq a \leq$ 30nm for aC grains and 40nm $\leq a \leq 1\mu$m for Si grains. aC grains condense out of 60 % of the ISM carbon abundance at temperatures below 2000 K, Si grains form out of the full ISM Si abundance below 1500 K. [(2)] λ1.3 mm total (CMP+ aC) opacity; [(3)] spectral index between λ3 and λ1.3 mm.

Table 6. FIR 5, spherically symmetric radiative transfer models

Dust Model [(1)]	$s^{(2)}$	$R_{\rm aC}^{(3)}$ [10^{13}cm]	$R_{\rm CMP}^{(3)}$ [10^{15}cm]	$R_{\rm out}$ [10^{16}cm]	$\langle n_{\rm H_2}\rangle_{\rm V}^{(4)}$ [10^8cm^{-3}]	$\langle T_{\rm D}\rangle^{(5)}$ [K]	$M_{\rm env}$ [M$_\odot$]	$L_{\rm bol}$ [L$_\odot$]	$S_{350\mu{\rm m}}$ [Jy]	$\frac{\Delta(\log(\tau_\nu))^{(6)}}{\Delta(\log(\nu))}$
low-luminosity models										
A	-1.5	2.7	1.5	2.8	2.3	16	50	1.6	32	1.0
B	-1.0	0.4	1.4	1.8	2.2	19	13	3.3	52	1.2
	-1.5	1.7	1.5	2.6	0.9	17	16	1.6	33	1.2
	-2.0	4.2	1.5	6.3	0.1	13	25	1.6	35	1.2
C	-1.5	0.7	1.7	2.8	2.3	18	50	4.1	57	1.0
D	-1.5	2.0	1.4	2.6	1.8	16	32	1.1	23	1.0
high-luminosity models										
A	-1.5	5.5	2.6	2.6	1.0	22	16	33	149	1.2
B	-1.5	3.4	2.7	2.5	0.3	23	5	33	161	1.4
C	-1.5	7.5	3.0	2.8	0.8	25	16	83	155	1.2
D	-1.5	4.2	2.6	2.6	0.5	23	8	33	147	1.3

Notes: [(1)] according to Table 5, [(2)] density profile $n_{\rm H_2} \propto r^s$, [(3)] $R_{\rm ac}$ amorphous carbon sublimation radius, $R_{\rm CMP}$ ice mantle sublimation radius, [(4)] volume averaged H_2 density, [(5)] mean dust temperature, weighted by dust λ1.3 mm emissivity, [(6)] opacity spectral index between λ3 mm and λ1.3 mm.

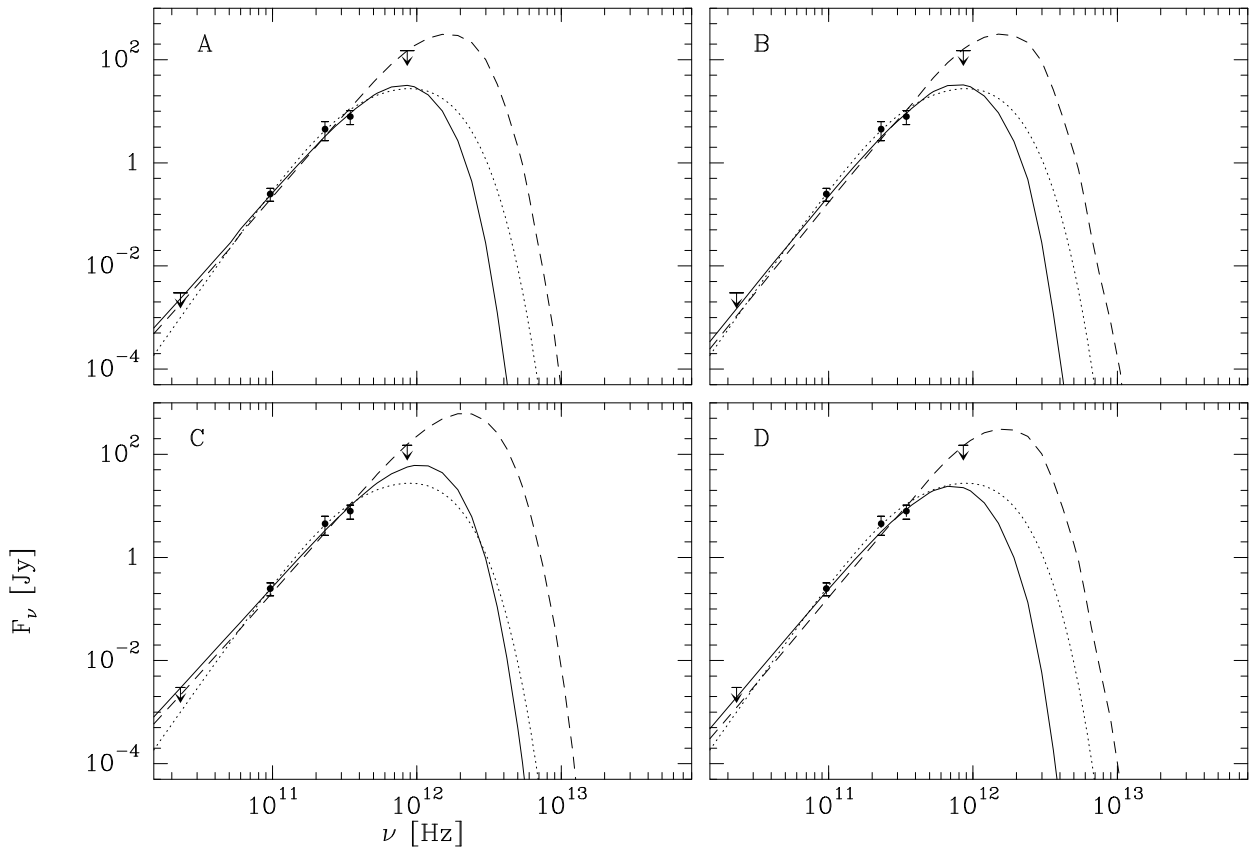

Fig. 6. Spectral energy distribution of the FIR 5 models, calculated by spherically-symmetric radiative transfer (models A-D for FIR 5-w, solid lines: low-luminosity models, dashed lines: high-luminosity models, see Table 6) and analytically for two isothermally cold (15 K) spheres (representing FIR 5-e and -w) at constant density (dotted lines, flux density from the FIR5 -e/w complex, see Table 4). Errorbars show the estimated flux uncertainty.

at shorter, more optically thick wavelengths that arises from the cool outer layers only (Table 6, Fig. 7).

Our best model fits all are characterized by low bolometric luminosities and high envelope masses ($13 - 50 M_\odot$, with $\langle n_{\rm H_2} \rangle_{\rm V} \sim 10^8$ cm^{-3}). Dust compositions with large ice coatings (models B and D, Table 5) ask for lower envelope masses (Table 6) due to their enhanced extinction cross sections. Within the observational uncertainties, the density gradient is poorly constrained, and a steeper profile can be compensated by a larger cut-off radius. However, because the mass is mainly determined by the long-wavelength fluxes, the final fit depends weakly on the assumed density law, and the variation is within the uncertainties implied by the various dust models. Allowing for external heating asks for a steeper density profile to compensate for the (excess) emission from (warmer) dust in the outer envelope layers. Because it appears difficult to quantify the effect of external heating (see Lis et al. 1991, for details), be it by the sources of energy in the H II region directly (in a clumpy environment, Graf et al. 1990) or by the re-processed radiation from the warm dust in the gas surrounding the protostellar cores (Schulz et al. 1991, Graf et al. 1990), we restrict our analysis to the case of an internally heated core, thus considering the deduced luminosities upper limits.

The low luminosity (low bulk temperature $\langle T_{\rm D} \rangle$, Table 6) required in this set of model fits is basically confined by the $\lambda 870$ μm data point, which value defines the turnover in the spectral energy distribution. In view of the critical consequences of the derived low L/M ratio on our interpretation of the core's state of evolution (see next section), we run a set of more luminous models that - while overestimating the flux at $\lambda 870$ μm - is constrained now by the upper flux density limit of 150 Jy at $\lambda 350$ μm [2], thus providing severe limits on the luminosity and envelope mass. The results, showing the large sensitivity of our models (namely of the luminosity) on the actual sub-mm flux, are summarized in Table 6.

Clearly, only with the availability of high-resolution (to avoid confusion with emission external to the cores) sub-mm fluxes, tracing the optically thick outer envelope, will it be possible to better discriminate between the models. A better char-

[2] An upper limit on the flux density from the FIR 5 point source, $S_\nu < 150$ Jy at 350 μm, has been derived from first measurements with the *Heinrich-Hertz-Telescope*, kindly provided by Robert Zylka (priv. comm.).

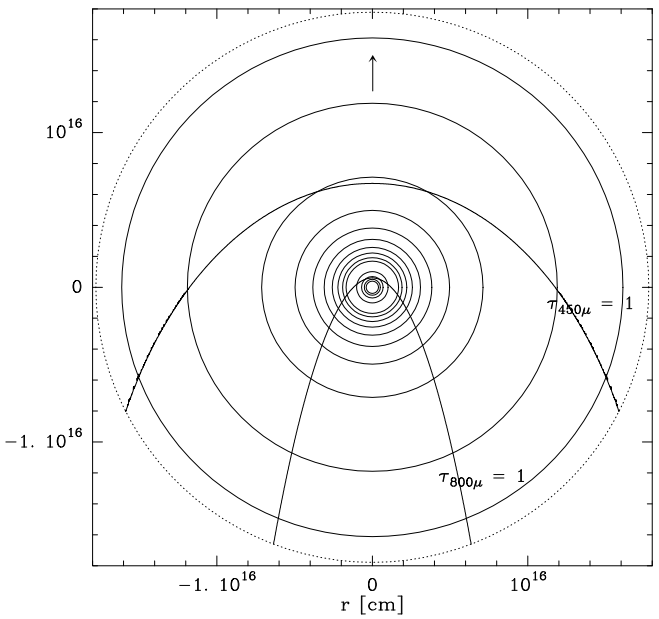

Fig. 7. Temperature structure and line-of-sight opacity of the dust envelope (model B, $s = -1.0$, contours of constant opacity $\tau_\lambda = 1.0$ at $\lambda 450$ μm and $\lambda 800$ μm). The arrow points to the observer. The dotted line is the outer boundary. The dust temperatures (averaged over the three dust components) are given by the contours (15, 20 to 100 by 10 K, 150 to 300 by 50 K).

acterization of the turnover of the spectral energy distribution, which likely becomes evident at $\lambda \sim 870$ μm, is indispensable to better determine the mass and luminosity of the envelope.

4.3. The nature of the dust condensations

We have analyzed in detail the continuum and line emission from the southern NGC 2024 cloud core. We have presented independent evidence that the embedded compact dust cores (with size of $\sim$ 1000 AU only) must be massive and ultra-dense ($\langle n_{\mathrm{H_2}} \rangle_{\mathrm{V}} \sim 10^8\,\mathrm{cm}^{-3}$, Table 6). The evidence is based on the cores' millimeter continuum emission, and on the dynamics of the surrounding molecular gas clumps - though the dust cores proper have not yet been detected in a molecular tracer (see below). The uncertainty of our model fits is dominated by (1) the poorly constrained SED, in particular the lack of high-resolution FIR/sub-mm measurements, (2) the range of dust properties, expected for grains covered by thick ice coatings, and (3) - although with lower sensitivity - by the unknown structure (i.e. the intrinsic density gradient of the the just barely resolved cores). For a given dust model, the envelope mass is determined within a factor of 3, but the luminosity may vary by as much as a factor of $10-20$ (Table 6). Within the set of (preferred) low-luminosity solutions, dust models with thick coatings (B, D) are in closer agreement with our dynamical mass estimate.

The early state of evolution of the cores is best characterized - in perspective to their envelope mass - by the rather low bolometric luminosity (see e.g. André & Montmerle 1994, André 1995). For FIR 5 we derive uniquely large $M_{\mathrm{env}}/L_{\mathrm{bol}}$ ratios, $\sim 10 - 30$, with an *absolute* lower limit of $\sim 0.2 - 0.5$ from the high-luminosity solutions (30 for FIR 6, respectively, from the isothermal model). Comparison with the luminosity predicted from the evolutionary tracks for low-mass protostars (e.g. Stahler 1983, Palla & Stahler 1991, and references therein) limits the mass of the central object to $\lesssim 1\,\mathrm{M}_\odot$(high luminosity limit) - if the star were close to the so-called "stellar birthline", where it becomes optically visible. More likely, in view of the high envelope masses deduced, the object still derives its energy from accretion, in which case its mass is described by

$$M_* \sim \frac{L_{\mathrm{bol}} R_*}{G\dot{M}} \sim 0.1 \left(\frac{10^{-5}\,\mathrm{M}_\odot \mathrm{yr}^{-1}}{\dot{M}} \right) \cdot \left(\frac{L_{\mathrm{bol}}}{10\,\mathrm{L}_\odot} \right) \mathrm{M}_\odot, \quad (6)$$

assuming R_* a few 10^{11} cm and $\dot{M} \sim 10^{-5}\mathrm{M}_\odot\mathrm{yr}^{-1}$ as characteristic estimates (Stahler 1983, Palla & Stahler 1991). Thus, the mass of the envelope exeeds by far the mass of any central object.

Amazingly, despite its early evolutionary state, the protostar seems associated with one of the most striking CO outflows known in the Galaxy (e.g. Richer et al. 1990). The mechanical luminosity stored in the outflow compares with the bolometric luminosity of the source, $L_{\mathrm{mech}} \sim 1 - 10 L_\odot$, which shows that right during the early accretion phase processes are at work to solve the angular momentum problem. The high momentum flux deposited in the CO flow (Richer et al. 1992) and our upper limit to the bolometric source luminosity place FIR 5 at the very beginning of the evolutionary tracks presented by Bontemps et al. (1996, their Fig. 5) for the outflow activity of low-mass embedded YSOs. [3]

As ultimate proof of the above scenario one would like to directly observe the kinematic footprint of the collapsing envelope by means of high-resolution molecular spectroscopy (Leung & Brown 1977). But as a matter of fact, so far nature has prevented us from detecting a molecular correspondence to the prominent dust cores. The striking offset between the $\lambda 3$ mm dust and $\mathrm{C^{34}S}$ $(2-1)$ line emission is seen in Figs.1 and 2. From the $3\,\sigma_{\mathrm{rms}}$ contours, we derive upper limits on the $\mathrm{C^{34}S}$ column density of $\sim 2 \times 10^{14}\,\mathrm{cm}^{-2}$ towards FIR 5 (at $T_{\mathrm{kin}} \sim 20$ K) and with the linewidth of any hypothetical spectral feature calculated assuming virial equilibrium with a clump mass of 16 $\mathrm{M}_\odot$, corresponding to low-luminosity model B in Table 6). Comparison with the $\mathrm{H_2}$ column densities deduced from spherically-symmetric radiative transfer modelling ($N_{\mathrm{H_2}} \sim 3 \times 10^{24}\,\mathrm{cm}^{-2}$, source averaged) yields a molecular abundance of $[\mathrm{C^{34}S}]/[\mathrm{H_2}] \sim 10^{-12}$, which, with respect to the fractional abundance determined for the molecular gas surrounding these dense cores, corresponds to a molecular underabundance by 3 orders of magnitude. The most likely explanation is the sensitivity of the CS abundance to freeze-out of elements onto the surface of dust grains (or as ice incorporated

[3] Similarly, following the classification scheme of André et al. (1993), in which the selective luminosity at $\lambda 1.3$ mm is used to characterize the state of evolution, $L_{\mathrm{bol}}/1000 \times L_{1.3\,\mathrm{mm}} \lesssim 10$ identifies these sources as higher mass equivalents of the low-mass Class 0 objects.

in fluffy grains; for details about the freeze-out timescale see Taylor et al. 1996, and references therein). In view of the luminosity limits deduced here, with therefore the bulk of the envelope mass at low temperature (Table 6), the differential, inversed temperature dependence between an optically thin thermalized molecular line emission, scaling by $\int(n_{C^{34}S}/T_{\rm gas})dl$, and the dust continuum emission, scaling by $\int(\sigma_\lambda^{\rm H} n_{\rm H} T_{\rm D})dl$, clearly cannot account for an anti-correspondence that strong (as suggested by e.g. Richer 1992 and Chandler & Carlstrom 1996).

At this point one may ask why we have failed (1) to detect the transition zone, where the CS abundance increases to its value deduced for the clump ensemble, and (2) to detect the dust continuum associated with the dense $C^{34}S$ clumps. The answer to the first question must be a steep density fall-off towards the edge of FIR 5, that separates the core from its surrounding medium and keeps the $C^{34}S$ column density too low to be detectable. In our above model fits to the continuum emission, this is reflected in the need for an outer cut-off radius $R_{\rm out}$. For comparison, we refer to a recent paper by Ward-Thompson (1996), who demonstrated that for pre-stellar low-mass cloud cores the density profile is inconsistent with a single, scale-free power law. The answer to the second question lies in the combined effects of spatial structure and sensitivity. Assuming that the continuum has an extent comparable to and a distribution as smooth as the velocity-integrated $C^{34}S$ emission, this contribution would be difficult to detect without zero spacing information (note that different to the line data, for the continuum observations no short spacings are available). Furthermore, the mass column densities derived for the gas clumps (Table 2) are about 2 orders of magnitude below those of the dust cores (Table 4), therefore the predicted continuum brightness falls short of the sensitivity limits of the current study (peak fluxes of a few mJy/beam are expected).

5. Conclusions

High-angular resolution observations (beam: $2'' \times 4''$) in the $\lambda 3$ mm continuum and the $C^{34}S\,(2-1)$ line emission have been used to study the morphological and kinematical fine-structure of the molecular cloud complex NGC 2024 (south). The main conclusions of this work are:

1. The dust continuum emission from the FIR 5 and FIR 6 cores (Mezger et al. 1988) has been resolved at 96 GHz. FIR 5 consists of at least two components, that are separated by $\sim$ 1700 AU. The main component, FIR 5-w, comprising $\sim 80\%$ of the flux density, is resolved with $\sim$ 1000 AU size. Higher resolution observations will reveal the true nature of the sources, be it a disk-envelope or simply a binary system.
2. The optically thin $C^{34}S$ line emission arises from two clump ensembles, close to and likely physically associated with the dust cores. However, NO line emission is detected on the line-of-sight towards these cores. The interclump velocity dispersion towards the northern clump ensemble yields a dynamical mass that exceeds the total clump mass by an order of magnitude. We conclude that the hidden mass is contained in the FIR 5 core, consistent with our mass estimates derived from the dust models (see below). The highly coherent velocity field observed in the southern ensemble was modelled in terms of a Keplerian streamer, which mass is negligible with respect to the central mass. Again, a dynamical mass is estimated that exceeds the observed gas mass by an order of magnitude, and attributes the dominant mass of the southern clump ensemble to FIR 6.
3. The spectral energy distribution (SED) and source size of FIR 5-w is analyzed in detail by means of a radiative transfer modelling in spherical symmetry, and allowing for a range of "appropriate" dust compositions (containing polluted ice mantles). The ambiguity of the physical solutions (namely, the envelope mass and the bolometric luminosity) is due to the lack of high-resolution FIR/sub-mm flux measurements; predictions for comparison with future sub-mm observations are presented that will help to better confine the core's properties. Our "low-luminosity" solutions, which fit the long-wavelength SED best, ask for low bolometric luminosities ($L_{\rm bol} \sim 1-4\,{\rm L}_\odot$) but massive envelopes ($10-50\,{\rm M}_\odot$); dust compositions allowing for thick ice coatings provide best agreement with our dynamical mass estimates. A recent flux density limit at $\lambda 350\,\mu$m constrains the bolometric luminosity to $L_{\rm bol} \lesssim 30-80\,{\rm L}_\odot$ and the envelope mass to $M_{\rm env} \gtrsim 5\,{\rm M}_\odot$, depending on the dust model. Comparison with protostellar evolution tracks implies that the envelope mass must exceed the mass of any (suspected) central object by order(s) of magnitude: the formation of the new star must be in its earliest phases of evolution, and -most likely- its energy is still derived from accretion.
4. Our high-resolution data ascertain the anti-correspondence between the dust continuum and molecular line emission towards FIR 5 and FIR 6. CS is estimated to be underabundant by as much as three orders of magnitude with respect to the surrounding gas clumps. This is most likely due to the high sensitivity of the CS abundance to freeze-out of elements onto dust grains, within this high-density environment ($\langle n_{\rm H_2}\rangle_{\rm V} \sim 10^8\,{\rm cm}^{-3}$). Albeit allowing for an internal heating source, the underabundance cannot be explained by thermal effects.

Acknowledgements. The authors benefited from discussions with C.M. Walmsley. T.L. Wilson and R. Zylka kindly provided results prior to publication. H.W. thanks Th. Preibisch for the coated grain models and for an initiation to the radiative transfer code. H.W. acknowledges support by the *Studienstiftung des deutschen Volkes*.

References

André, P., Ward-Thompson, D., Barsony, M., 1993, ApJ 406, 122
André, P., Montmerle, T., 1994, ApJ 420, 837
André, P., 1995, Ap&SS 224, 29
Anthony-Twarog, B.J., 1982, AJ 87, 1213
Barnes, P.J., Crutcher, R.M., Bieging, J.H., Storey, J.W.V., Willner, S.P., 1989, ApJ 342, 883
Barnes, P.J., Crutcher, R.M., 1990, ApJ 351, 176
Beckwith, S.V.W., Sargent, A.I., Chini, R.S., Güsten, R., 1990, AJ 99, 924
Bertoldi, F., McKee, C.F., 1992, ApJ 395, 140

Blake, G.A., Sutton, E.C., Masson, C.R., Phillips, T.G., 1987, ApJ, 315, 621
Bontemps, S., André, P., Terebey, S., Cabrit, S., 1996, A&A 311, 858
Cabrit, S., Bertout, C., 1986, ApJ 307, 313
Chandler, C.J., Carlstrom, J.E., 1996, ApJ 466, 338
Gaume, R.A., Johnston, K.J., Wilson, T.L., 1992, ApJ 388, 489
Genzel, R., Downes, D., 1977, A&AS 30, 145
Goldreich, P., Kwan, J., 1974, ApJ 189, 441
Graf, U.U., Genzel, R., Harris, A.I., Hills, R.E., Russell, A.P.G., Stutzki, J., 1990, ApJ 358, L49
Guilloteau, S., Forveille, T., 1992, *Grenoble Image and Line Data Analysis System* (GILDAS), Version 2.0
Guilloteau, S. et al., 1992, A&A 262, 624
Lada, E.A., Bally, J., Stark, A.A., 1991, ApJ 368, 432
Leung, C.M., Brown, R.L., 1977, ApJ 214, L73
Lis, D.C., Carlstrom, J.E., Phillips, T.G., ApJ 370, 583
Lucas, R., 1992, *Continuum and Line Interferometer Calibration* (CLIC), Version 2.2
Mathis, J.S., Rumpl, W., Nordsieck, K.H., 1977, ApJ 217, 425
Mauersberger, R., Wilson, T.L., Mezger, P.G., Gaume, R., Johnston, K.J., 1992, A&A 256, 640
McKee, C.F., Zweibel, E.G., 1992, ApJ 399, 551
Mezger, P.G., Chini, R., Kreysa, E., Wink, J.E., Salter, C.J., 1988, A&A 191, 44
Mezger, P.G., Wink, J.E., Zylka, R., 1990, A&A 228, 95
Mezger, P.G., Sievers, A.W., Haslam, C.G.T., Kreysa, E., Lemke, R., Mauersberger, R., Wilson, T.L.W., 1992, A&A 256, 631
Palla, F., Stahler, S.W., 1992, ApJ 392, 667
Preibisch, Th., 1992, Diplom thesis, Julius-Maximilians-Universität Würzburg
Preibisch, Th., Ossenkopf, V., Yorke, H.W., Henning, Th., 1993, A&A 279, 577
Richer, J.S., 1990, MNRAS 245, 24p
Richer, J.S., Hills, R.E., Padman, R., 1992, MNRAS 254, 525
Sanders, D.B., Willner, S.P., 1985, ApJ 293, L39
Schulz, A., Güsten, R., Zylka, R., Serabyn, E., 1991, A&A 246, 570
Stahler, S.W., 1983, ApJ 274, 822
Stutzki, J., Güsten, R., 1990, ApJ 356, 513
Sutton, E.C., Peng, R., Danchi, W.C., Jaminet, P.A., Sandell, G., Russell, A.P.G., 1995, ApJS, 97, 455
Taylor, S.D., Morata, O., and Williams, D.A., 1996, A&A in press
Thronson, H.A., Lada, C.J., Schwartz, P.R., Smith, H.A., Smith, J., Glaccum, W., Harper, D.A., Loewenstein, R.F., 1984, ApJ 280, 154
Ward-Thompson, D., 1996, Ap&SS 239, 151
Wilson, T.L., Mehringer, D.M., Dickel, H.R., 1995, A&A 303, 840
Wilson, T.L., Gaume, R.A., Johnston, K.J, Schmidt-Burgk, J., 1996, in proc. of the ESO conference on *Science with Large Millimeter Arrays*, ed. P. Shaver, in press
Yorke, H.W., 1980, A&A 86, 286
Yorke, H.W., Shustov, B.M., 1981, A&A 98, 125

This article was processed by the author using Springer-Verlag LaTeX A&A style file *L-AA* version 3.